POLAR SCIENCE

Complex mesoscale landscapes beneath Antarctica mapped from space

Helen Ockenden[1,2]*, Robert G. Bingham[2]*, Daniel Goldberg[2], Andrew Curtis[2], Mathieu Morlighem[3]

The landscape shrouded by the Antarctic Ice Sheet provides important insights into its history and influences the ice response to climate forcing. However, knowledge of this critical boundary has depended on interpolation between irregularly distributed geophysical surveys, creating major spatial biases in maps of Antarctica's subglacial landscape. As stress changes associated with ice flow over bedrock obstacles produce ice surface topography, recently acquired, high-resolution satellite maps of the ice surface offer a transformative basis for mapping subglacial landforms. We present a continental-scale elevation map of Antarctica's subglacial topography produced by applying the physics of ice flow to ice surface maps and incorporating geophysical ice thickness observations. Our results enrich understanding of mesoscale (2 to 30 kilometers) subglacial landforms and unmask the spatial distribution of subglacial roughness and geomorphology.

Despite being identified by the Intergovernmental Panel on Climate Change (IPCC) as a crucial boundary condition for projections of global sea level rise (*1*, *2*), less is known about the topography beneath the ice of Antarctica than any other planetary surface in the inner solar system (*3*–*6*). Understanding of the shape and composition of Antarctica's bed has traditionally come from airborne and ground-based geophysical surveys, which although extensive, have not been acquired systematically across the ice sheet. In many regions the spacing between survey tracks remains at 10 to 100 km (*7*, *8*), much greater than the kilometer resolutions that models require to predict future sea level with low uncertainties (*9*–*12*).

In well-confined, fast-flowing ice streams, mass conservation has been used to map topography between survey lines. In the interior of Antarctica, however, existing maps of subglacial topography use interpolation techniques such as kriging, adapted plate spline interpolation (Bedmap3) (*8*) and streamline diffusion (BedMachine v3) (*13*). In regions away from survey tracks, these techniques have not been able to reproduce the roughness of subglacial terrain observed along radar profiles or mesoscale landscapes truly analogous to those exposed by deglaciation of former ice sheets (*14*–*16*). Some studies have used statistical interpolation techniques such as in-painting or super-resolution (*17*–*19*) to simulate subglacial topography with realistic roughness, but maps produced with statistical techniques have not been widely applied in ice sheet modeling as they do not always satisfy physical laws.

An alternative approach, facilitated by the development of modern satellite remote sensing technology, is to apply inverse methods to high-resolution observations of the ice surface. We employed an inverse method termed Ice Flow Perturbation Analysis (IFPA) (*20*, *21*) that leverages the physics of ice flow to invert for subglacial topography from contemporary ice surface datasets (*22*–*24*). Previous studies that have applied IFPA to data from Thwaites Glacier (*20*) and Pine Island Glacier (*21*) have shown that IFPA can reproduce the pattern of subglacial hills and valleys seen in recent ice-penetrating radar surveys. More details about the IFPA method, its known limitations, and how these have been addressed in this work can be found in the methods and supplementary text.

Using limited ice thickness measurements (*13*), we produced a map of subglacial topography that captures the mesoscale nature and roughness of the landscape (IFPA*meso*) but also contains some long-wavelength offsets to geophysical survey observations. We therefore applied an additional correction to produce a second map (IFPA) which simultaneously includes the novel mesoscale details and is consistent with all the available geophysical data (see methods). The new IFPA map deploys ice physics (based on the full Stokes equations of ice flow) across the entirety of Antarctica's interior and reveals a diversity of new mesoscale landscape details.

New windows into mesoscale landscape variability

Our IFPA map of Antarctica's subglacial landscape (Fig. 1) shows mesoscale (2 to 30 km) topographic variability across the continent with unprecedented detail (Fig. 1B, Fig. 2, and figs. S11 to S28). Newly identified features or those resolved with substantially greater detail than before include incised valleys (Fig. 2, A to C), topographic boundaries or lineations likely to have a geological or tectonic origin (Fig. 2, D and E), and topographic details in subglacial highlands (Fig. 2, F to H).

In Maud Subglacial Basin, we find a steep-sided channel incised into the subglacial substrate, with average depth 50 m and width ~6 km, running for nearly 400 km (Fig. 2A), which we hypothesize may be connected to drainage systems from the mountains of Dronning Maud Land. In Wilhelm II Land, we find evidence for a set of unsurveyed channels cutting across substantial ridges (Fig. 2B), with dimensions similar to those of sub-ice sheet channels previously identified elsewhere by airborne radar surveys (*25*–*27*). From their surface expression, these channels have been hypothesized to form part of an extensive hydrological system draining from Subglacial Lake Qilin (*28*, *29*). Our map also reveals incised valleys across higher-elevation blocks, such as Hercules Dome, where several deep valleys cut across the subglacial plateau (Fig. 2C). These valleys are similar to "U-shaped" glacial valleys imaged nearby with multi-element swath radar, which have been interpreted to represent alpine glaciation in an initiation zone for ice sheet growth (*30*). Additional definition is added to channels in the Slessor Glacier Basin, Blackwall Glacier Trough, and between Highlands B and C (figs. S14.8, S14.7, and S26.32 respectively).

The IFPA-derived subglacial topography effectively captures sharp edges in basal topography that may characterize geological boundaries, as exemplified in Recovery Subglacial Basin (Fig. 2D). Radar surveys of the basin have shown that there is a region of raised topography in the center of the basin (*31*), flanked by lower ground in which sits a series of subglacial lakes (*32*, *33*). The lowlands versus highlands have broadly been interpreted from gravity and magnetic surveys to represent sedimentary basins versus crystalline massifs (*34*), but the wide spacing of the radar tracks had left the boundary between the two geological regions poorly resolved. Our map clearly picks out a sharp, linear transition between the two terrains (Fig. 2D). Further insight into subglacial geology is provided around East Antarctica's Zhigalov Subglacial Mountains, where the more finely resolved subglacial topography shows multiple features following a consistent strong north-south trend (Fig. 2E). Further west in the more intensively aerogeophysically surveyed Dronning Maud Land, similar north-south–trending landforms have been attributed to Paleozoic to Mesozoic rifting (*35*). We also see a much clearer outline of the boundary between Astrolabe Subglacial Basin and Porpoise Subglacial Highlands (fig. S25.29), as well as previously unresolved topographic structures along the crests of those highlands. The IFPA

[1]L'Institut des Géosciences de l'Environnement, Université Grenoble-Alpes, Saint-Martin-d'Hères, France. [2]School of GeoSciences, University of Edinburgh, Drummond Street, Edinburgh, UK. [3]Department of Earth Sciences, Dartmouth College, Hanover, NH, USA
***Corresponding author. Email: helen.ockenden@univ-grenoble-alpes.fr (H.O.); r.bingham@ed.ac.uk (R.G.B.)**

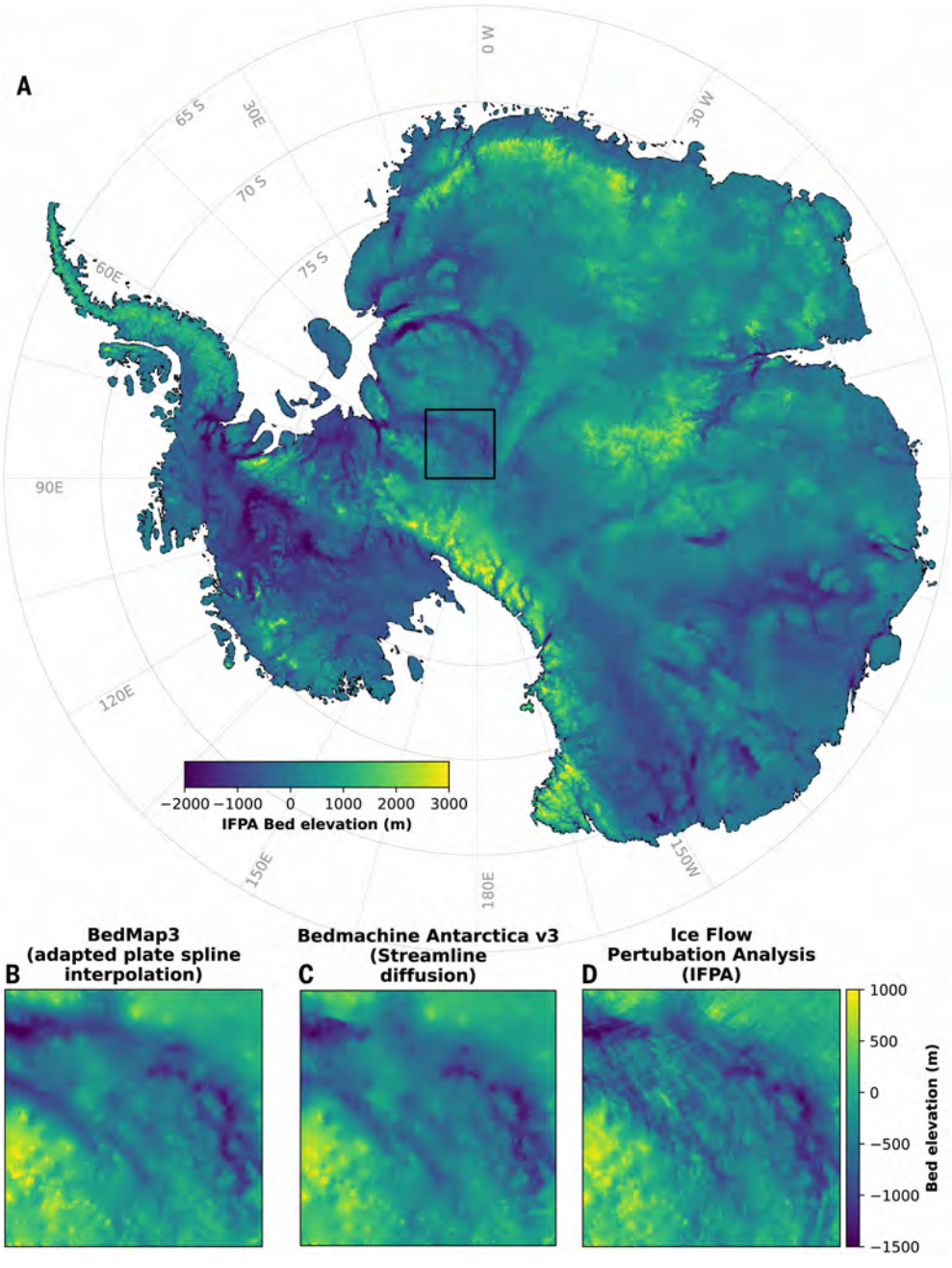

Fig. 1. IFPA subglacial topography of Antarctica. (**A**) shows the IFPA subglacial topography for the whole Antarctic continent and (**B** to **D**) show a comparison of different bed topography maps for the Pensacola-Pole Basin region [outlined in black on (A). (B) displays Bedmap3 (*8*), (C) displays BedMachine Antarctica v3 (*13*), and (D) displays IFPA subglacial topography. The map production workflow is detailed in the methods; the main input datasets include the Gapless REMA ice-surface digital elevation model (*24*), the MEaSURES Antarctic ice-velocity product (*23*), the BedMachine Antarctica v3 bed-elevation map (*13*), and all available geophysical survey measurements of ice thickness from Bedmap3 (*7*) and CReSIS SAR surveys (*59*). A considerably higher resolution version of (A) is available on Zenodo (*57*).

map identifies some small topographic features in the depths of Astrolabe Subglacial Basin, supporting the suggestion by geophysical surveys that subglacial water in the region is most likely not concentrated into a single lake but rather distributed across a more marsh-type environment (*36*).

We also resolve the mesoscale landscapes of Antarctica's subglacial highlands with unprecedented clarity for all of Antarctica's most poorly surveyed regions. For example, across highland blocks flanking East Antarctica's deep subglacial basins, we detect geometric features that resemble alpine valleys cutting across the highlands (Fig. 2, F and G). In the Highland A region, where these features have been surveyed by airborne radar, they have been interpreted as a preserved paleo-river landscape (*27*); our map shows a widespread distribution of these features across the continent's highlands. The new map also unmasks numerous new dendritic valley-ridge complexes thought to be diagnostic of alpine glaciation in other sparsely surveyed subglacial highlands of East Antarctica, such as the Golicyna Subglacial Mountains (Fig. 2H) (*37*).

The texture of Antarctica's ice sheet bed

To quantify the mesoscale subglacial landscape textures described above across the whole Antarctic continent, we applied a range of metrics to the IFPA map (methods). For comparison, we also applied these techniques to two of the most recently available bed Digital Elevation Models (DEMs): BedMachine Antarctica v3 (*13*) and Bedmap3 (*8*), which use streamline diffusion and adapted plate spline interpolation, respectively, to interpolate between geophysical surveys. The spatial pattern in texture obtained from the IFPA map contrasts strongly with those shown for the interpolated DEMs (Fig. 3), in which the spatial variability corresponds far more closely to the uneven distribution of ice-penetrating radar observations (Fig. 3C and S7). Our results give a new overview of the pancontinental subglacial landscape and allow us to generate the first picture of the texture of the entire Antarctic bed that leverages the physics of ice flow and high-resolution ice surface datasets to significantly reduce bias from geophysical survey density.

As a measure of mesoscale (2 to 30 km) topographic variability and a proxy for subglacial roughness, we consider the distribution of subglacial hills (defined as local maxima with at least 50 m of topographic prominence in a 5-km neighborhood). We identify twice as many subglacial hills in the IFPA topography map (71,997) than are counted in BedMachine Antarctica v3 (36,346), (Fig. 3A). The Bedmap3 hill count falls between these two values, but at mesoscale resolution it is highly influenced by ice thickness survey locations (fig. S7). We also see higher fractal dimensions (a spectral measure of topographic roughness at different length scales, sometimes linked to basal drag) (*15*, *38*) in the IFPA map (Fig. 3B), especially in regions where we know from geophysical surveying that there is elevated, rough topography. Alongside the topography map, these roughness

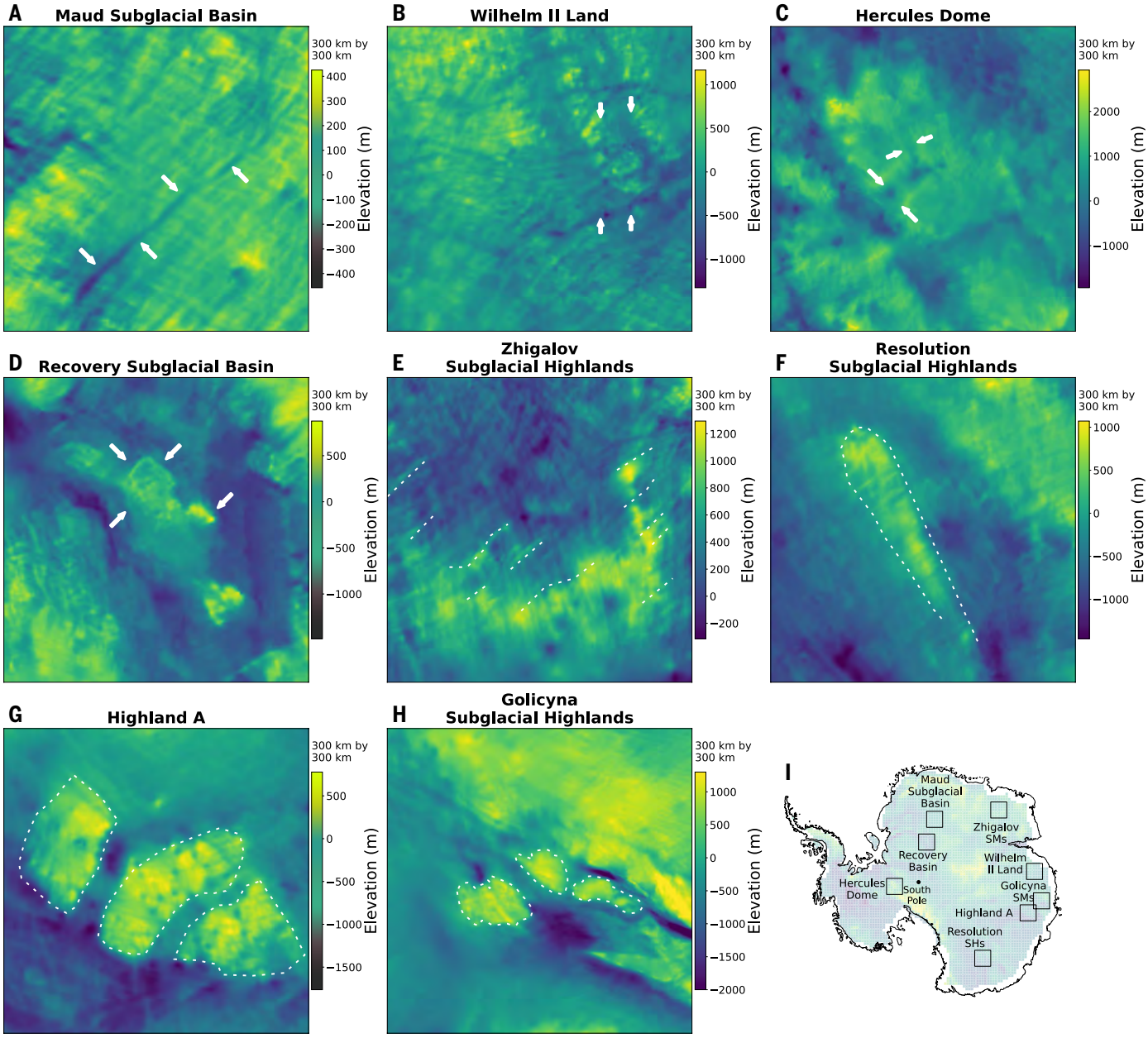

Fig. 2. Selected examples of new IFPA subglacial topography. (**A** to **C**) Examples of channels incised into the subglacial substrate; (**D** and **E**) improved definition of subglacial topographic lineations likely related to tectonics; and (**F** to **H**) newly defined topography in subglacial highlands. Note that the panels vary in size from 100 × 100 km to 300 × 300 km. (**I**) Panel locations. Key linear features are annotated with white arrows and area features are outlined with dotted white lines. See supplementary figures for examples shown alongside topography from BedMachine Antarctica v3 (*13*) and Bedmap3 (*8*), as follows: Maud Subglacial Basin (fig. S16.11), Hercules Dome (fig S13.5), Recovery Subglacial Basin (fig. S16.12), Zhigalov Subglacial Highlands (figs. S24.28 and S28.36), Resolution Subglacial Highlands (fig. S22.23), Highland A (fig.S26.32), Golicyna Subglacial Highlands (fig. S27.34).

metrics may provide important insights into basal drag, a key boundary condition for ice sheet models.

The landscape beneath Antarctica's ice

Research on formerly glaciated landscapes has demonstrated that broad-scale relationships exist between the nature of the landscape and its glacial history (*39*–*41*). High-relief alpine landscapes are produced by cirque and valley glaciers in elevated regions, at the beginning and end of glaciations (*42*, *43*). Low-relief landscapes [such as central northern Canada (*39*) and coastal Scandinavia (*44*)] have been inferred to represent ubiquitous erosion (previously termed areal scouring) beneath unconstrained ice flow with abundant subglacial meltwater, during peak glaciation. In regions with variable hydrological conditions, landscapes of "selective erosion" develop, in which terrains of low-relief high ground (protected from erosion due to basal freezing) are dissected by deeply eroded glacial troughs (recording where water and thus erosion occurred at some time) (*45*, *46*).

Using selected example regions of low-relief, alpine, and selectively eroded topography, as well as the textural characteristics detailed in the methods, we made a simple division of the landscape of Antarctica into regions by topographic style. As we focused on

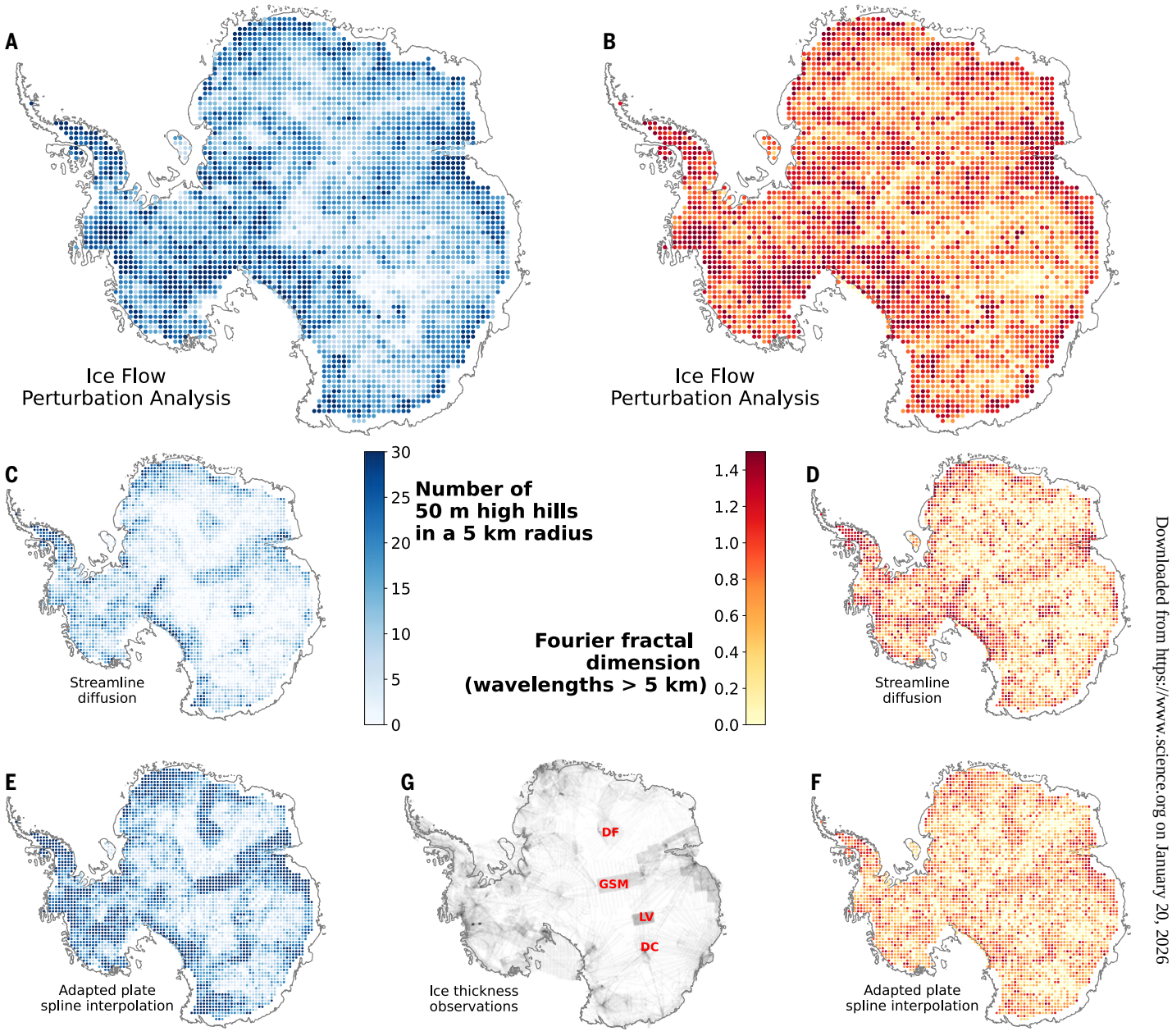

Fig. 3. The texture of Antarctica's ice sheet bed. (**A**, **C**, and **E**) Number of 50-m hills within a 5-km radius and (**B**, **D**, and **F**) Fourier fractal dimension for wavelengths >5 km (a proxy for subglacial landscape roughness), extracted from (A) and (B) IFPA topography, (C) and (D) topography interpolated between geophysically derived bed picks using streamline diffusion (BedMachine Antarctica v3) (*13*), and (E) and (F) an adapted plate spline interpolation (Bedmap3) (*7*,*8*). Each pixel represents a 50 km × 50 km region. (**G**) Locations of bed picks used to derive both interpolated topographies (From Bedmap3 thickness survey count) (*8*). The most densely surveyed regions of East Antarctica are annotated: DF, Dome Fuji; GSM, Gamburtsev Subglacial Mountains; LV, Lake Vostok; DC, Dome C. Note the significant correspondence between the spatial patterns in interpolated topographies (C) and (E) and geophysical survey locations (G). By contrast, (A) and (B) show that with IFPA we can now calculate subglacial landscape texture across Antarctica consistently, without major bias from geophysical survey locations.

metrics of mesoscale texture, the characteristics employed for this classification were calculated using the IFPA*meso* map to give a self-consistent picture of the subglacial landscape and reduce the effect of uneven geophysical survey spacing. This is the first landscape classification applied to a subglacial DEM produced primarily from ice surface datasets, and the first to reveal landscape dynamics across the whole continent including for regions away from geophysical survey lines.

Although all major subglacial mountain ranges in Antarctica have already been identified in previous studies (*37*, *47*, *48*), the greater revelations of our IFPA*meso*-guided classification lie in the respective distributions of low-relief and selectively eroded landscapes, which deviate from previous mapping and interpretations. Notably, we identify fewer regions of low-relief topography. In part this is because many of the areas identified (*42*) as having low-relief subglacial topography in 2014 ("areal scour") were located in gaps between radar surveys (e.g., Princess Elizabeth Land, central Dronning Maud Land, and the South Pole Basin), and were naturally, albeit erroneously, recorded as flatter ground than our IFPA*meso* analysis shows. Our classification clarifies that most of Antarctica's low-subglacial relief

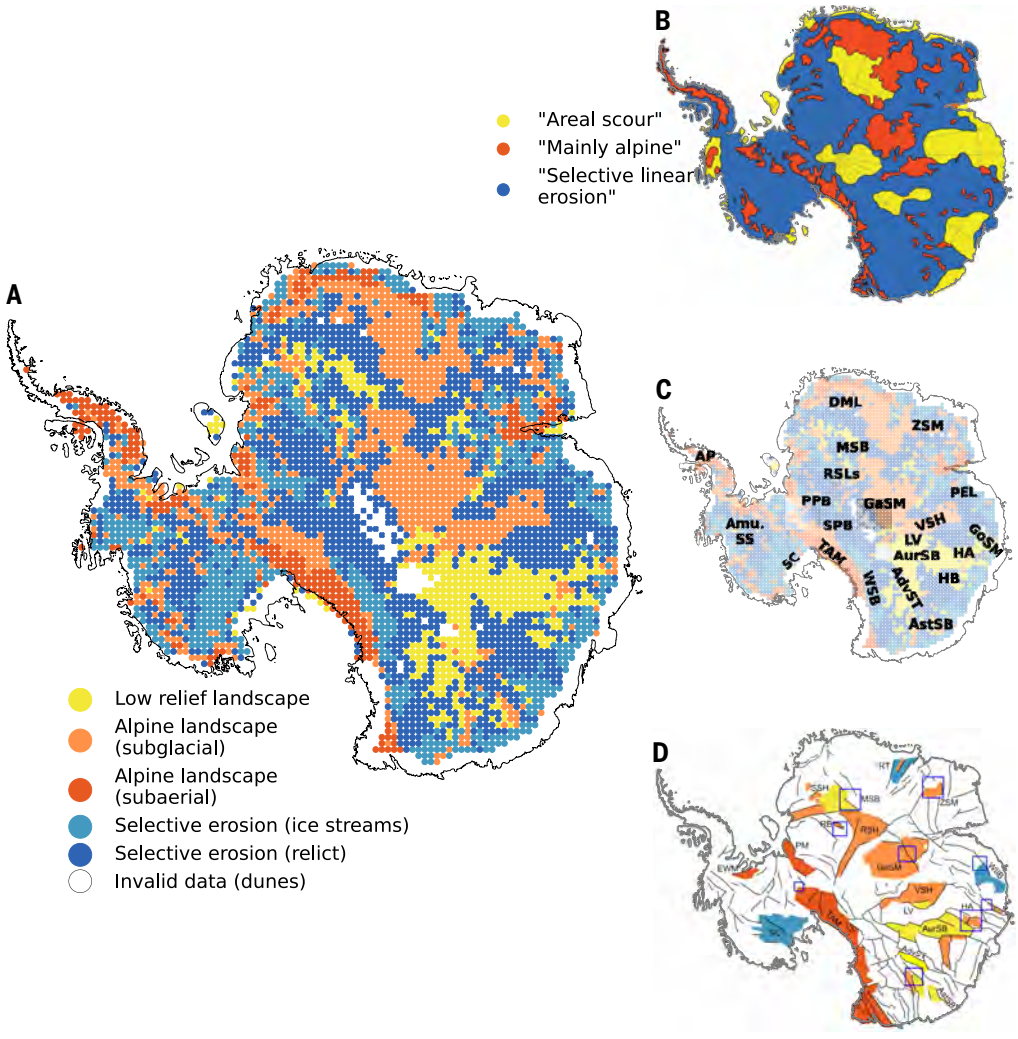

Fig. 4. Geomorphological classification of Antarctica's subglacial landscape. (**A**) Application to IFPA*meso* subglacial topography. (**B**) Previous classification applied in 2013 to interpolated bed topography (Bedmap2) (*60*), adapted from Jamieson *et al*. (*42*). In each panel the classification shows regions of low-relief, alpine (both fully submerged–subglacial and partially submerged–subaerial) and selectively eroded landscapes. (**C**) Locations discussed in text. (**D**) Locations of tectonic boundaries across Antarctica, adapted from (*34*). We have colored some examples of regions where the geological structure mirrors the tectonic structures that we see. Adv. ST, Adventure Subglacial Trench; Amu. SS, Amundsen Sea Sector; AP, Antarctic Peninsula; Ast SB, Astrolabe Subglacial Basin; Aur SB, Aurora Subglacial Basin; DML, Dronning Maud Land; EWM, Ellsworth Mountains; GaSM, Gamburtsev Subglacial Mountains; GoSM, Golicyna Subglacial Mountains; HA, Highland A; HB, Highland B; LV, Lake Vostok; MSB, Maud Subglacial Basin; PEL, Princess Elizabeth Land; PM, Paxutent Mountains; PPB, Pensacola-Pole Basin; RT, Ragnhild Trough; RSH, Recovery Subglacial Highlands; RSLs, Recovery Subglacial Lakes; SC, Siple Coast; SPB, South Pole Basin; WIIB, Wilhelm II Basin; WSB, Wilkes Subglacial Basin; ZSM, Zhigalov Subglacial Mountains.

regions are in central East Antarctic basins thought to contain deep sedimentary infills (*49*, *50*) and confined by tectonic boundaries observed in magnetic and gravity surveys (e.g., Aurora Subglacial Basin, Adventure Subglacial Trench, and Maud Subglacial Basin, Fig. 4D). Low-relief landscapes are also seen in regions previously identified as containing a high density of subglacial lakes [e.g., Recovery Subglacial Lakes (*32*) and Astrolabe Subglacial Basin (*51*)]. Our classification reimagines the interpretation of the lowest-relief subglacial topography in the interior of Antarctica, suggesting that substantial landscapes of areally scoured bedrock are likely to be rare in actively glaciated regions, and that in the interior these landscapes instead represent wide-ranging regions of sedimentary infill. However, this does not mean that there are not landscapes of areal scour present, only that more sophisticated methods are required to identify them.

In our textural classification, areas collectively termed as resulting from selective erosion cover 56% of Antarctica and describe any topography that is not clearly low-relief or alpine. We further identified a subclass of these regions, with high RMS slope and low fractal dimension (methods), geographically clustered around present-day ice streams such as those along the Siple Coast (figs. S12.3 and S12.4b), the Amundsen Sea Sector, and the Pensacola-Pole Basin. This allowed us to distinguish between areas where we hypothesize erosion is an active modern day process and areas where the relict landscape of selective erosion is preserved in the absence of major ice streams and variable ice flow today (figs. S25.30 and S27.33). These preserved landscapes may reflect multiple phases of past ice sheet growth and retreat of a less extensive Antarctic Ice sheet, most likely before the mid-Miocene (14 million years ago) (*52*). Radio-echo soundings from Highland B (*53*) confirm the presence of landscapes where deep troughs selectively breach uplands around ice sheet margins, and there are numerous analogs around the fringes of East Greenland and various Arctic ice caps (*54*–*56*).

Mapping a way ahead

Our IFPA map of Antarctica's subglacial landscape reveals that an enormous level of detail about the subglacial topography of Antarctica can be inverted from satellite observations of the ice surface, especially when combined with ice thickness observations from geophysical surveys (*7*, *13*). We have used the map to illustrate the step forward we have taken in our understanding of the mesoscale (2 to 30 km) topography beneath Antarctica, exploring selected examples of the landscape features that it uncovers, and showing that previous topographic maps have been limited by bias toward geophysical survey locations. Additionally, from the mesoscale texture of this new topography, we have interpreted primary glacial geomorphological regimes across the Antarctic continent and thus provided insights for developments in the process of understanding of ice sheet history and future ice sheet dynamics.

Although IFPA cannot resolve features that are shorter in length than the ice thickness, because flow over these features does not induce any perturbations in the ice surface, landscapes tend to have fractal roughness structures (*15*), meaning that the mesoscale textures that we identify will be correlated with small-scale roughness and can provide

information about ice flow regimes (*38*). Our landscape classification and topographic map therefore serve as important guides toward more focused studies of Antarctica's subglacial landscape, informing where future detailed geophysical surveys should be targeted, as well as the extents and resolutions (e.g., flight-track spacing) required to capture the fine details required for ice flow modeling.

REFERENCES AND NOTES

1. Intergovernmental Panel on Climate Change (IPCC), "The Ocean and Cryosphere in a Changing Climate: Special Report of the Intergovernmental Panel on Climate Change" (Cambridge Univ. Press, 2022); https://doi.org/10.1017/9781009157964.
2. Intergovernmental Panel on Climate Change (IPCC), "9 – Ocean, Cryosphere and Sea Level Change" (Cambridge Univ. Press, 2023); https://doi.org/10.1017/9781009157896.011.
3. K. Gwinner *et al.*, *Earth Planet. Sci. Lett.* **294**, 506–519 (2010).
4. R. R. Herrick, D. L. Stahlke, V. L. Sharpton, *Eos* **93**, 125–126 (2012).
5. K. J. Becker *et al.*, "First global digital elevation model of Mercury" in *47th Annual Lunar and Planetary Science Conference* (2016); pp. 2959.
6. Y. Yu, D. T. Sandwell, G. Dibarboure, *Science* **386**, 1251–1256 (2024).
7. A. C. Frémand *et al.*, *Earth Syst. Sci. Data* **15**, 2695–2710 (2023).
8. H. D. Pritchard *et al.*, *Sci. Data* **12**, 414 (2025).
9. G. Durand, O. Gagliardini, L. Favier, T. Zwinger, E. le Meur, *Geophys. Res. Lett.* **38**, L20501 (2011).
10. S. Sun, S. L. Cornford, Y. Liu, J. C. Moore, *Cryosphere* **8**, 1561–1576 (2014).
11. F. McCormack, B. Galton-Fenzi, H. Seroussi, J. Roberts, The impact of bed elevation resolution on Thwaites Glacier ice dynamics. *Twenty-Fifth Annual WAIS Workshop* (2018).
12. B. A. Castleman, N.-J. Schlegel, L. Caron, E. Larour, A. Khazendar, *Cryosphere* **16**, 761–778 (2022).
13. M. Morlighem *et al.*, *Nat. Geosci.* **13**, 132–137 (2020).
14. M. Margold, C. R. Stokes, C. D. Clark, *Earth Sci. Rev.* **143**, 117–146 (2015).
15. K. A. Hogan *et al.*, *Cryosphere* **14**, 2883–2908 (2020).
16. F. A. M. Falcini, M. Krabbendam, K. A. Selby, D. M. Rippin, *J. Glaciol.* **68**, 518–532 (2022).
17. E. MacKie, D. Schroeder, J. Caers, M. Siegfried, C. Scheidt, . *J. Geophys. Res. Earth Surf.* **125**, e2019JF005420 (2020).
18. W. J. Leong, H. J. Horgan, *Cryosphere* **14**, 3687–3705 (2020).
19. Y. Cai *et al.*, *IEEE Trans. Geosci. Remote Sens.* **61**, 1–17 (2023).
20. H. Ockenden, R. G. Bingham, A. Curtis, D. Goldberg, *Cryosphere* **16**, 3867–3887 (2022).
21. H. Ockenden, R. G. Bingham, A. Curtis, D. Goldberg, *J. Glaciol.* **69**, 1–10 (2023).
22. I. M. Howat, C. Porter, B. E. Smith, M.-J. Noh, P. Morin, *Cryosphere* **13**, 665–674 (2019).
23. J. Mouginot, E. Rignot, B. Scheuchl, *Geophys. Res. Lett.* **46**, 9710–9718 (2019).
24. Y. Dong, J. Zhao, C. Li, M. Liao, *ISPRS J. Photogramm. Remote Sens.* **186**, 70–82 (2022).
25. K. C. Rose *et al.*, *Geology* **42**, 971–974 (2014).
26. S. J. Livingstone, W. Chu, J. C. Ely, J. Kingslake, *Geology* **45**, 551–554 (2017).
27. S. S. R. Jamieson *et al.*, *Nat. Commun.* **14**, 6507 (2023).
28. S. S. R. Jamieson *et al.*, *Geology* **44**, 87–90 (2016).
29. X. Cui *et al.*, *Earth Syst. Sci. Data* **12**, 2765–2774 (2020).
30. A. O. Hoffman *et al.*, *Nat. Geosci.* **16**, 1–9 (2023).
31. R. E. Bell, M. Studinger, C. A. Shuman, M. A. Fahnestock, I. Joughin, *Nature* **445**, 904–907 (2007).
32. A. Humbert, D. Steinhage, V. Helm, S. Beyer, T. Kleiner, *J. Geophys. Res. Earth Surf.* **123**, 2802–2826 (2018).
33. A. Diez *et al.*, *J. Geophys. Res. Earth Surf.* **124**, 287–304 (2019).
34. A. R. A. Aitken *et al.*, *Reviews of Geophysics* **61**, e2021RG000767 (2023).
35. O. Eisen, A. Winter, D. Steinhage, T. Kleiner, A. Humbert, *Ann. Glaciol.* **61**, 162–175 (2020).
36. D. W. Ashmore, R. G. Bingham, *Antarct. Sci.* **26**, 758–773 (2014).
37. E. J. Lea, S. S. Jamieson, M. J. Bentley, *Cryosphere* **18**, 1733–1751 (2024).
38. C. Schoof, *J. Glaciol.* **48**, 407–416 (2002).
39. D. E. Sugden, B. S. John, *Edward Arnold London* **365**, 1–363 (1976).
40. M. J. Siegert, J. Taylor, A. J. Payne, *Global Planet. Change* **45**, 249–263 (2005).
41. S. Franke *et al.*, *Earth Surf. Process. Landf.* **46**, 2728–2745 (2021).
42. S. S. Jamieson *et al.*, *Antarct. Sci.* **26**, 724–741 (2014).
43. C. Lambiel, B. Maillard, M. Kummert, E. Reynard, *J. Maps* **12**, 160–172 (2016).
44. O. Fredin *et al.*, *Nat. Commun.* **8**, 14879 (2017).
45. D. Sugden, *J. Glaciol.* **20**, 367–391 (1978).
46. A. M. Hall, K. Ebert, J. Kleman, A. Nesje, D. Ottesen, *Geology* **41**, 1203–1206 (2013).
47. F. Ferraccioli *et al.*, New aerogeophysical survey targets the extent of the West Antarctic Rift System over Ellsworth Land. in *10th International Symposium on Antarctic Earth Sciences*. A. K. Cooper, C. R. Raymond, Eds. (USGS, 2007); Extended Abstract 113, pp. 1–10.
48. T. T. Creyts *et al.*, *Geophys. Res. Lett.* **41**, 8114–8122 (2014).
49. A. Baranov, A. Morelli, A. Chuvaev, *Front. Earth Sci. (Lausanne)* **9**, 722699 (2021).
50. A. R. A. Aitken *et al.*, *Geophys. Res. Lett.* **41**, 2390–2400 (2014).
51. M. J. Siegert, N. F. Glasser, *Polar Res.* **16**, 63–72 (1997).
52. D. E. Sugden, S. S. Jamieson, *Scott. Geogr. J.* **134**, 203–223 (2018).
53. D. A. Young *et al.*, *Nature* **474**, 72–75 (2011).
54. H. Holtedahl, *Geogr. Ann., Ser. A* **49**, 188–203 (1967).
55. O. H. Løken, D. Hodgson, *Can. J. Earth Sci.* **8**, 185–195 (1971).
56. D. Sugden, *Landscapes of Glacial Erosion in Greenland and their Relationship to Ice, Topographic and Bedrock Conditions* (Univ. of Aberdeen, 1974); 177–195.
57. H. Ockenden, Data accompanying manuscript: Complex mesoscale landscapes beneath Antarctica mapped from space, v3, Zenodo (2025); http://dx.doi.org/10.5281/zenodo.15223468.
58. H. Ockenden, hockenden97/Antarctic_subglacial_topo: Minor edits to figures, v4.0.0, Zenodo (2025); https://zenodo.org/records/17601672.
59. CReSIS, Center for Remote Sensing of Ice Sheets (CReSIS) radio-echo sounding data repository, Open Polar Data Centre (2025); https://data.cresis.ku.edu/data/rds/.
60. P. Fretwell *et al.*, *The Cryosphere* **7**, 375–393 (2013).

ACKNOWLEDGMENTS

This research has only been made possible through the many colleagues behind the acquisition, analysis, and open publication of the underpinning satellite datasets. In particular, we acknowledge DigitalGlobe (now Maxar Technologies); WorldView and GeoEye programmes for REMA; JAXA's ALOS; ESA's Envisat and ERS; NASA's Landsat; CSA's RADARSAT programmes for MEaSUREs; University of Minnesota's NSF-funded Polar Geospatial Data Center for REMA; NASA and NSIDC for MEaSUREs; and the provision and open publication of six decades of geophysical dataset acquisition across Antarctica by multiple colleagues in the Scientific Committee for Antarctic Research Bedmap consortium. To all of these colleagues, we extend our gratitude and appreciation. The authors also thank S. Jamieson and G. Paxman for valuable comments on an early draft and the two referees of this paper, whose reviews significantly improved the final manuscript. **Funding:** This research was supported by the Natural Environment Research Council (NERC) E4 Doctoral Training Partnership (grant NE/S007407/1), the International Thwaites Glacier Collaboration (ITGC, grant nos. NERC NE/S006672, NERC NE/S006621/1, NERC NE/S006613/1, NERC NE/S006796/1, NSF PLR 1738934), and the Evans Family Fellowship (through a postgraduate fellowship for H.O. to visit Dartmouth College), and the ANR AIAI project (ANR-22-CE01-0014). This is ITGC Contribution No. ITGC-161. **Author contributions:** Conceptualization: H.O., R.G.B., D.G., and A.C.; Code development and mapping: H.O. and M.M.; Analysis & interpretation: H.O. and R.G.B.; Visualization: H.O.; Writing (original draft): H.O. and R.G.B.; Writing (review & editing): H.O., R.G.B., D.G., A.C., and M.M. **Competing interests:** The authors declare no competing interests. **Data, code, and materials availability:** The IFPA map dataset and other datasets required to produce the figures in this manuscript are available on Zenodo (*57*). The code used to generate the IFPA map presented here, and the figures in this manuscript, is available on GitHub and (*58*). All other data needed to evaluate the conclusions in the paper are present in the paper or the supplementary material. No samples or new materials were collected or generated for this study.

SUPPLEMENTARY MATERIALS

science.org/doi/10.1126/science.ady2532
Methods; Supplementary Text; Figs. S1 to S28; References (*61–80*)

Submitted 15 April 2025; accepted 25 November 2025

10.1126/science.ady2532